ORIGINAL PAPER

Insights into impact simulation and fatigue analysis of thermoplastically jointed lapshear specimens

Janko Kreikemeier[1] · Steffen Opitz[1]

Abstract

The development process of an aircraft fuselage today shows a complex workflow from the first concept phase to the actual operational phase. On one hand, this has a direct impact on the efficiency of both the short-term ramp-up of aircraft production and long-term robustness. On the other hand, this prevents disruptive ideas for innovative architectures with integrated functionalities that enable significant mass savings, cost reduction, increased operational efficiency and the reduction of CO_2 and NOx emissions. The ICASUS (ICASUS-Integrated Cabin-Airframe-System Fuselage, funded by European Joint Undertaking Clean Sky 2 No. JTI-CS2-CPW-LPA-02-01.) project focuses on the development of disruptive concepts and methodologies for an integrated airframe architecture in the cabin/cargo system and fuselage. For this purpose, an integrated approach was developed throughout the entire fuselage from the initial concept to the final operational phase, which directly takes into account several future functionalities and complex requirements from different disciplines. Technologies for future multifunctional structures have been developed to be applied to large-scale modules, future aircraft factories and customization aspects. Furthermore, the development of a novel thermoplastic material was significantly supported by DLR's (DLR-Deutsches Zentrum für Luft- und Raumfahrt e. V./German Aerospace Center.) simulation and experimental material and subcomponent tests. This paper provides insights into numerical investigations of lapshear specimens subjected to impacts with varying energies. The main focus was on simulating the impact itself, as well as conducting subsequent fatigue and residual strength analyses.

1 Notation

Throughout the text, a direct tensor notation is preferred. If necessary, an index notation using the summation convention will be used to avoid the definition of new conventions. Vectors are denoted by lowercase bold letters $a = a_i e_i$ where e_i denote the orthonormal base vectors. A second order tensor is represented by an uppercase bold letter $A = A_{ij} e_i \otimes e_j$. Tensors of fourth order are called tetrads and are symbolised by $\mathbb{C}$. The dyadic product is defined as $(a \otimes b) \cdot c = (b \cdot c)a$. A single scalar contraction is denoted by a dot. In case of more than one scalar contraction, the number of dots corresponds to the number of vectors that are contracted, e.g., $\alpha = A \cdot \cdot B$. The dot is omitted if only one scalar contraction takes place, e.g., $a = Ab$.

2 Introduction

The current development process of aircraft fuselages follows a complex workflow, extending from the initial conceptual phase to the final operational phase. Within this process, three distinct categorical streams have been established for airframe, cabin/cargo, and systems development. While this organizational structure contributes to clarity, it also presents challenges to efficiency, impacting both short-term production ramp-up and long-term robustness. Additionally, this segmentation hampers the emergence of disruptive ideas for innovative architectures with integrated functionalities, which have the potential

✉ Janko Kreikemeier
  janko.kreikemeier@dlr.de

  Steffen Opitz
  steffen.opitz@dlr.de

1 German Aerospace Center, Institute of Lightweight Systems, Lilienthalplatz 7, 38108 Braunschweig, Lower Saxony, Germany

to offer significant benefits such as weight reduction, cost efficiency, increased operational efficiancy, and reduced emissions of CO2 and NOx. The ICASUS project aims to address these challenges by focusing on the development of disruptive concepts and methodologies for an integrated airframe architecture encompassing the cabin/cargo system and fuselage. To achieve this, ICASUS adopts an integrated approach throughout fuselage development, from initial concept to final operational phases. This holistic perspective considers multiple future functionalities and complex requirements across different disciplines. Specifically, ICASUS works on developing and validating specific enabler technologies for future multifunctional structures, targeting elementary parts, subcomponents, modules, interfaces, and customization aspects. By doing so, ICASUS seeks to enable the realization of more disruptive concepts characterized by heightened integration and robustness, thus avoiding costly late-stage modifications or encountering unknown certification hurdles. The anticipated outcomes of the ICASUS project include the development of a Functional and Operational Requirements Catalogue serving as a certification baseline, alongside a disruptive Fuselage Airframe Architecture featuring newly developed integration approaches. Moreover, the project aims to deliver a Material Options Catalogue, Advanced Manufacturing Means, a comprehensive Technology Verification and Validation Plan, and a Means of Compliance Assessment, accompanied by estimations illustrating the potential for weight savings, reduced production costs, and enhanced operational efficiency associated with future integrated airframe architectures. Carbon fiber reinforced thermoplastic polymers (CFRTP) have emerged as promising materials for aerospace applications due to their excellent material properties, including weight-specific stiffness and strength. Unlike thermoset matrix materials, thermoplastic matrix materials offer superior damage tolerance properties, simpler processing, ease of recycling, and do not require expensive cooling for storage. Of particular interest is the joining of CFRTP structures, with thermoplastic welding offering fast and cost-effective joining processes. The failure behavior of CFRTP structures and thermoplastic joining zones has been extensively researched, with various mathematical models developed to describe and evaluate failure mechanisms. In the aviation industry, traditional joining processes such as mechanical riveting and thermosetting bonding are primarily used. However, thermoplastic matrix systems offer alternative joining processes, including welding technologies and fusion bonding technologies, which present promising alternatives to traditional methods. The continuous development and optimization of thermoplastic welding processes are essential to meet the growing demand for thermoplastic composite materials in the aerospace industry.

This study investigates the failure behavior of thermoplastically jointed lapshear connections with and without pre-existing impact damage at various impact energies through numerical analysis. Special attention is given to post-impact fatigue behavior and subsequent examination of residual strength. Finite element models equipped with cohesive contacts at the respective junctions are developed to accurately represent the initiation and propagation of damage within the connection zones. The findings of this study contribute to understanding material failure within thermoplastic bonding zones and inform the development of more robust joining techniques for aerospace applications. Similar examinations on L-Pull models have been previously conducted in [1], demonstrating that the numerical models can adequately depict the onset of failure and the propagation of damage.

The mathematical description and evaluation of the failure behaviour of CFRTP structures and especially of the thermoplastic joining zones has been the subject of research for several decades. Starting with the relatively simple analytical approaches, such as equivalent stress criterion, maximum principal stress or strain criteria, the interpolation criterion offers for the first time the possibility to evaluate multiaxial loads in a single layer or in a complete laminate, [2]. By [3], a further very accepted failure criterion was introduced, which allows the distinction between fiber and interfiber breakage by evaluating the current load in the fracture process zone. With the introduction of stress intensity factors by [4], cracks in mechanical structures were characterized for the first time. The differentiation of the different fracture modes based on stress, planar shear and non-planar shear finally led to the definition of three different stress intensity factors. At the same time, this can be seen as a starting point for linear elastic fracture mechanics (LEFM). The disadvantage of all mathematical models from the field of LEFM must be seen in the stress singularities at the respective crack tip. It is known that a plastic zone is formed at the crack tip, which limits the resulting stresses. The description of ductile material behaviour at the crack tip was introduced by [5] through the crack tip opening displacement concept (CTOD). For ductile materials, it is assumed that the crack behavior depends only on the plastic deformations at the crack tip. The concept can be seen as the starting point for Elastic Plastic Fracture Mechanics (EPFM). In [6, 7] were the first to implement the idea of further developing the crack tip into a fracture process zone in order to avoid stress singularities. By doing so, cohesive forces act on the fracture process zone until the crack opening has reached a critical

value. The cohesive forces then degrade until the crack surfaces are finally stress-free and the crack can spread further. At the same time, the concept of the Cohesive Zone Method was born. The description of the formation of discontinuities with discrete interface elements was mainly driven by [8–10] and [11]. For an overview of the numerical implementation of the cohesive zone approach within the framework of the finite element method, this paper mainly gives [10, 12–16] and [17].

Thermoplastic matrix systems enable the application of alternative joining processes. In the aviation industry, where mechanical riveting processes or duroplastic bonding processes are primarily used today, thermoplastic matrix systems also permit the use of welding technologies or fusion bonding technologies. The following disadvantages must be considered for mechanical riveting and thermosetting bonding processes: While stress concentrations occur at the rivet holes during mechanical riveting, complex surface preparation is usually indispensable for the thermosetting bonding of structural components. In contrast, thermoplastic welding processes, such as electric resistance welding, ultrasonic welding or electromagnetic induction welding, offer promising alternatives to these joining processes, [18] and the references therein. The continuous further development and optimization of thermoplastic welding processes is an important component today, since the demand for thermoplastic composite materials in the aerospace industry is also constantly growing in comparison with metallic and thermoset materials, in order to be able to better withstand the static and fatigue loads in the structure.

3 Modelling of interlaminar failure

The cohesive zone model (CZM) can be used to model composite separation in laminates. The basis for the CZM was provided by [19, 7]. According to his understanding, crack surfaces are located at a very close distance to each other, which is why interatomic forces can act, as shown schematically in Fig. 1.

At a distance of x_o, atoms or molecules are at the energetic minimum and are thus in equilibrium of forces. If an external load brings the system out of its equilibrium position, intermolecular forces counteract the load. The intermolecular forces increase with increasing atomic distance until they reach a maximum value and then fall back to a minimum. Contact or interface elements are used in order to be able to map this interaction relationship or this constitutive behaviour in the interface as well. Traction represents the stress or cohesive tension between the interfaces, while separation defines the opening gap of the interfaces. Contact or interface elements are created between the contact surfaces. In contrast to contact elements, interface elements have a finite thickness and are used, for example, when the adhesive seam of an adhesive bond is to be mapped geometrically. There are different traction-separation laws, which essentially have three characteristic features. The first characteristic relates to the stiffness behaviour of the cohesive zone model in the undamaged state. The second feature concerns the limit for the onset of damage, which is determined by the parameter τ^0 or t_n^0. The onset of damage is immediately followed by the softening range, which characterises the course of damage until complete failure and represents the

Fig. 1 Upper diagram: Potential energy versus atomic distance/molecular distance; Lower diagram: First derivative or interaction force versus atomic distance/molecular distance; Right: Schematic representation of the cohesive zone of a generic shape with crack
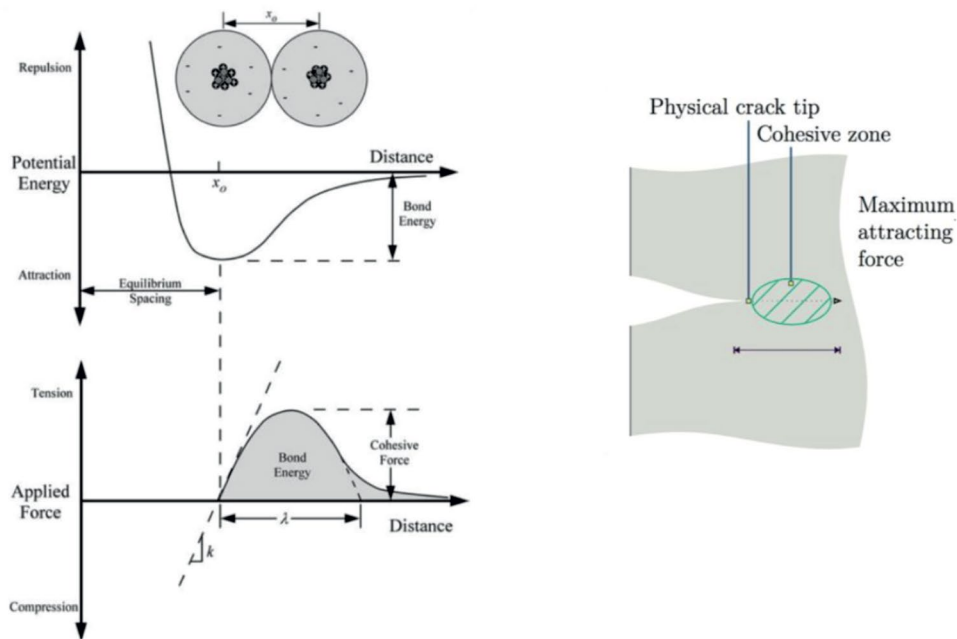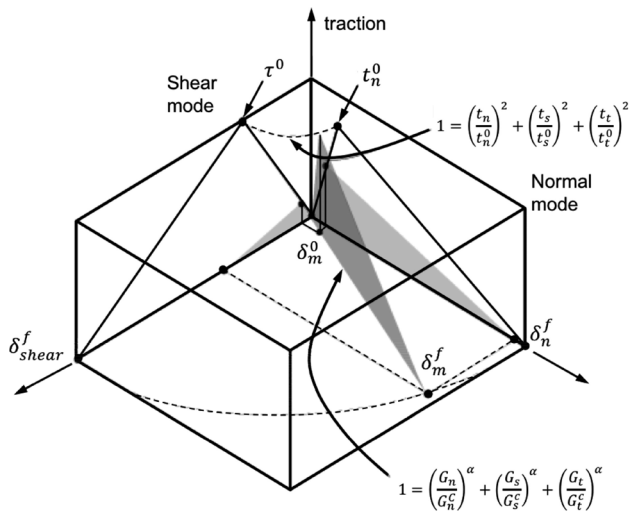
Fig. 2 Graphical representation of the bilinear mixed-mode traction-separation law in Abaqus

last feature. In the present work, contact elements are used which are assigned a bilinear traction-separation law, Fig. 2.

The quadratic nominal stress criterion is chosen as the damage initiation criterion

$$1 = \left(\frac{t_n}{t_n^0}\right)^2 + \left(\frac{t_s}{t_s^0}\right)^2 + \left(\frac{t_t}{t_t^0}\right)^2. \tag{1}$$

If the right side of the equation takes the value 1, damage occurs. The parameter t_n^0 represents the maximum normal stress and the parameters t_s^0 and t_t^0 represent the maximum shear stresses in the contact plane. Complete damage is present as soon as the power law criterion is fulfilled

$$1 = \left(\frac{G_n}{G_n^C}\right)^\alpha + \left(\frac{G_s}{G_s^C}\right)^\alpha + \left(\frac{G_t}{G_t^C}\right)^\alpha. \tag{2}$$

Here, G_n^C, G_s^C and G_t^C are the critical fracture energies in normal and tangential direction. The softening process is described via

$$D = \frac{\delta_m^f(\delta_m^m ax - \delta_m^0)}{\delta_m^m ax(\delta_m^f - \delta_m^0)}, \tag{3}$$

where δ_m^f represents the opening gap at complete failure and $\delta_m^m ax$ represents the maximum opening gap that has ever occurred in the load history.

4 Modelling of intralaminar failure

To model the intralaminar damage of elastic-brittle materials, which is especially true for UD laminates, Abaqus offers the Hashin damage model. According to Hashin's

understanding, four different material damage initiation mechanisms are to be considered for modelling damage initiation and progression. These concern

- fibre cracking in the longitudinal direction of fibre tension
- fibre buckling and buckling in the longitudinal direction of fibre compression
- matrix cracking under transverse tension and shear, and
- matrix fracture under transverse compression and shear

The mathematical criteria to model the damage onset are

Longitudinal tension $\hat{\sigma}_{11} \geq 0$:

$$F_f^t = \left(\frac{\hat{\sigma}_{11}}{X^T}\right)^2 + \alpha\left(\frac{\hat{\tau}_{12}}{S^L}\right)^2$$

with $\qquad$ (4)

X^T Tension strength in longitudinal direction

S^L Shear strength in longitudinal direction

α Coefficient of shear stress ratio

Longitudinal compression $\hat{\sigma}_{11} < 0$:

$$F_f^t = \left(\frac{\hat{\sigma}_{11}}{X^C}\right)^2$$

with $\qquad$ (5)

X^C Comp. strength in longitudinal direction

Transverse tension $\hat{\sigma}_{22} \geq 0$:

$$F_m^t = \left(\frac{\hat{\sigma}_{22}}{Y^T}\right)^2 + \alpha\left(\frac{\hat{\tau}_{12}}{S^L}\right)^2$$

with $\qquad$ (6)

Y^T Transverse tension strength

Transverse compression $\hat{\sigma}_{22} < 0$:

$$F_m^c = \left(\frac{\hat{\sigma}_{22}}{2S^T}\right)^2 + \left[\left(\frac{Y^C}{S^T}\right)^2 - 1\right]\frac{\hat{\sigma}_{22}}{Y^C} + \left(\frac{\hat{\tau}_{12}}{S^L}\right)^2$$

with $\qquad$ (7)

S^T Transverse shear strength

Y^C Transverse compression strength

where damage initiates if one of these criteria equals 1. The subsequent damage progress is characterised by a decrease in the acting stresses. A linear stress decrease is used, the qualitative course of which can be seen in a comparative stress-displacement diagram, Fig. 3.

The stress drop is realised mathematically by introducing the damage variables d_f, d_m and d_s within the damage

Fig. 3 Linear softening after damage initiation
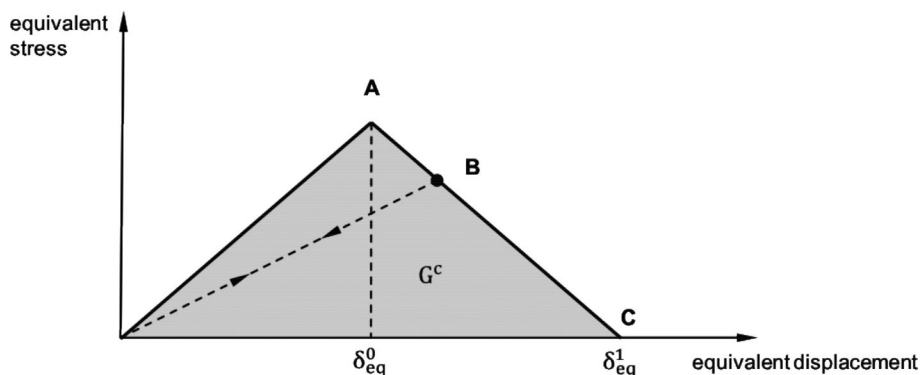
elasticity tetrad $\mathbb{C}_d$ given in Voigt notation[1] C_d of the material law. These damage variables can assume a value between 0 and 1. A value of 0 applies to the undamaged state (before damage initiation), while a value of 1 describes the complete failure of the material.

$$\boldsymbol{\sigma} = \boldsymbol{C}_d \cdot \boldsymbol{\varepsilon}, \tag{8}$$

$$C_d = \frac{1}{D}\begin{bmatrix} (1-d_f)E_1 & (1-d_f)(1-d_m)\nu_{21}E_1 & 0 \\ (1-d_f)(1-d_m)\nu_{12}E_2 & (1-d_m)E2 & 0 \\ 0 & 0 & (1-d_s)GD \end{bmatrix}, \tag{9}$$

$$D = 1 - (1-d_f)(1-d_m)\nu_{12}\nu_{21}, \tag{10}$$

$$d_f = \begin{cases} d_f^t & \text{if } \hat{\sigma}_{11} \geq 0 \\ d_f^c & \text{if } \hat{\sigma}_{11} < 0 \end{cases}, \tag{11}$$

$$d_m = \begin{cases} d_m^t & \text{if } \hat{\sigma}_{22} \geq 0 \\ d_m^c & \text{if } \hat{\sigma}_{22} < 0 \end{cases}, \tag{12}$$

$$d_s = 1 - (1-d_f^t) - (1-d_f^c) - (1-d_m^t) - (1-d_m^c). \tag{13}$$

5 Modelling of cyclic failure

The determination of the small damage progress per load cycle over many cycles leads to a very high calculation effort in transient analyses, even with relatively small FE models. To avoid this, the Direct Cycling (DC) approach can be used in Abaqus/Standard. With the DC approach, the response of a structure subjected to a periodic load can be determined with sufficient accuracy under reasonable computational effort. The basis of the approach is the assumption that the stress–strain relationship of any structure remains unchanged

after a certain number of cycles. This means that from the mentioned number of cycles, at time t_n, the stress–strain relationship of the structure is comparable to that at time t_{n+1}. The state for which the stress–strain relationship of the structure does not change is called the stable response of the system. The aim of the DC approach is to determine the stable response of the system. To do this, as in transient analyses, the structure can be subjected to a periodic load until the stable state is reached. However, this approach carries the risk of high computational effort, since the stable state may only occur after many cycles. To avoid this risk, the DC approach determines the stable response directly. A displacement function using Fourier-coefficients is used

$$\bar{\boldsymbol{u}}(t) = \boldsymbol{u}_0 + \sum_{k=1}^{n} \left[u_k^s \sin(k\omega t) + u_k^c \cos(k\omega t) \right]. \tag{14}$$

This displacement function is used to mathematically describe the structural response at all times t and is updated after each iteration using the modified Newton–Raphson method. Each pass through an entire load cycle is considered an iteration of the solution to the nonlinear problem. The update of the displacement function continues until the
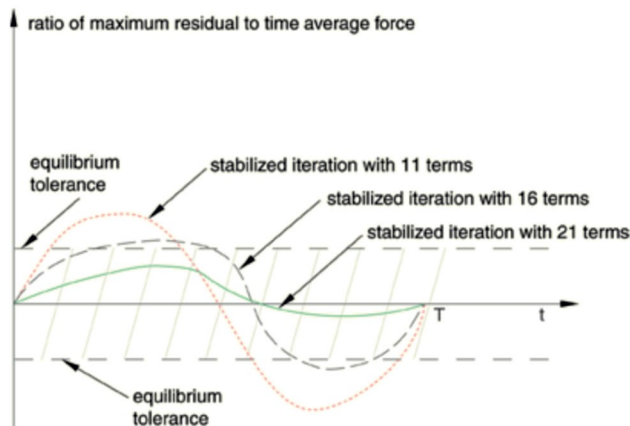
Fig. 4 Influence of number of Fourier terms on the convergence

---

convergence criterion is reached. The convergence criterion is fulfilled when the ratio of the residual and the force averaged over time is smaller than the preset tolerance value. Figure 4 shows this qualitatively under the influence of the number of Fourier terms (input parameters in Abaqus). An increase in the number of Fourier terms increases the solution accuracy, but this is also accompanied by a higher calculation effort and greater memory requirements. The number of Fourier terms is increased internally starting from the adjustable start value in Abaqus up to an adjustable end value, in case no convergence is achieved after n iterations.

The DC approach offers the possibility to simulate interlaminar and intralaminar damage and failure processes due to periodic loads. For this purpose, the low-cycle fatigue analysis option must be included or activated, which is only available in Abaqus/Standard. With the low-cycle fatigue analysis option, the structural response determined with the DC approach is used. Using this structural response, the damage progression or the reduced elasticity of the material is determined at discrete points and extrapolated within

the next load increment. Here, the load increment denotes a number of load cycles ΔN, Fig. 5.

This process is repeated until a statement on the service life can be made. There are two approaches to simulating the initiation and progression of damage in low cycle fatigue analysis. The first approach is suitable for tough materials, because in this continuum mechanical approach the cumulative plastic hysteresis deformation energy, Fig. 6, serves as the basis for calculating the damage initiation and the damage progress.

The second approach is based on linear elastic fracture mechanics with the extended finite element method. This

Fig. 7 Fatigue crack growth rate da/dN as a function of the cyclic energy release rate ΔG

Fig. 5 Material stiffness as function of number of cycles

Fig. 6 Qualitative stress–strain curve of a ductile material under cyclic load
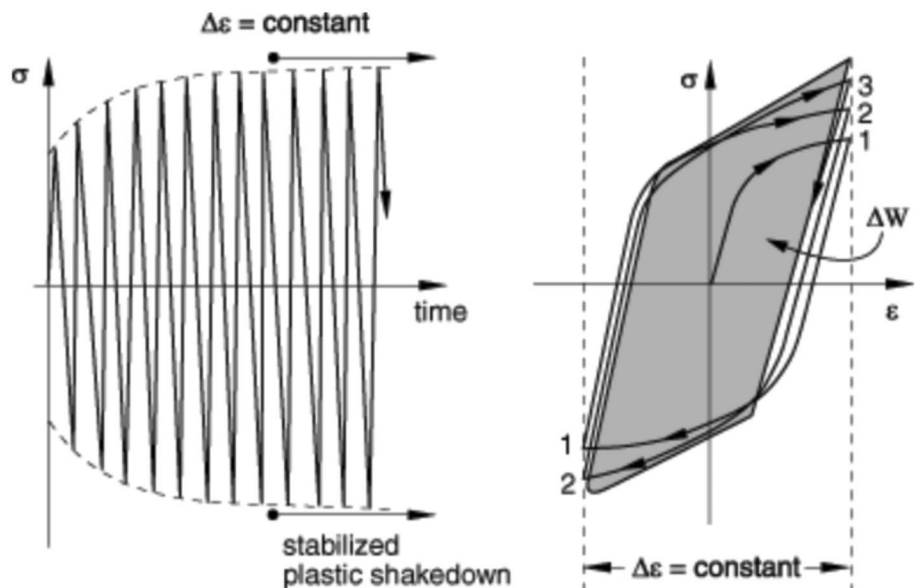
approach is used in this master thesis and is suitable for brittle materials. The calculation of damage initiation and propagation is based on the Paris–Erdogan law, [20], which describes the relationship between the energy release rate G and the crack propagation rate da/dN, Fig. 7.

A crack only starts to grow when the threshold value ΔG_{thres} is reached. The associated and implemented crack propagation is linear in the double logarithmic representation. At ΔG_{pl}, unstable crack growth occurs, which is characterised by an exponential increase in the rate of crack propagation. As the cyclic energy release rate continues to increase, the critical energy release rate ΔG_C is reached, which is accompanied by complete failure. The energy release rate is calculated as

$$G = -\frac{\partial(U + W)}{\partial a}. \tag{15}$$

Here $\partial(U + W)$ is the released energy (elastic energy and work of external forces) at crack extension ∂a. The cyclic energy release rate can be calculated according to

$$\Delta G = G_{\max} - G_{\min} = -\frac{\Delta K^2}{E} \tag{16}$$

with

$$\Delta K = \Delta\sigma\sqrt{\pi a}Y^*. \tag{17}$$

The energy release rate at the crack tip is determined internally using the VCCT technique. In Abaqus/Standard, the following criterion for the start of crack growth is implemented

$$f = \frac{N}{c_1 \Delta G^{c_2}} \geq 1, \tag{18}$$

where c_1 and c_2 are material constants and N is the number of cycles. After the crack growth initiation criterion has been met, the crack propagation rate da/dN can be calculated via

$$\frac{da}{dN} = c_3 \Delta G^{c_4} \tag{19}$$

with c_3 and c_4 as material constants. With a given number of oscillations N, Abaqus/Standard can thus determine the crack extension da with a load increment dN. Since in the FE models of this work there is no pure fracture mode I, fracture mode II or fracture mode III loading, but a mixed-mode loading, a further regularity must be included with which a scalar comparison quantity G_{equiv} can be determined. In this work, the Benzeggagh–Kenane formulation is used, [21], which is based on

$$G_{\mathrm{equivC}} = G_{\mathrm{IC}} + \left(G_{\mathrm{IIC}} - G_{\mathrm{IC}}\right)\left(\frac{G_{\mathrm{II}} + G_{\mathrm{III}}}{G_{\mathrm{II}} + G_{\mathrm{II}}G_{\mathrm{II}}}\right)^{\eta}. \tag{20}$$

With this comparative quantity, the failure condition according to

$$1 \leq f \leq 1 + f_{\mathrm{tol}}, \quad \text{with} \quad f = \frac{G_{\mathrm{equiv}}}{G_{\mathrm{equivC}}},$$
$$G_{\mathrm{equiv}} = G_I + G_{II} + G_{III} \tag{21}$$

can be assessed, where failure occurs as soon as f assumes a value greater than or equal to one. Unless $f \geq 1 + f_{tol}$ holds, the time step to fulfil the failure condition is shortened, except in the case of unstable crack growth.

Fig. 8 Calculation procedure for investigating the static residual load-bearing capacity and the fatigue residual load-bearing capacity after impact loads
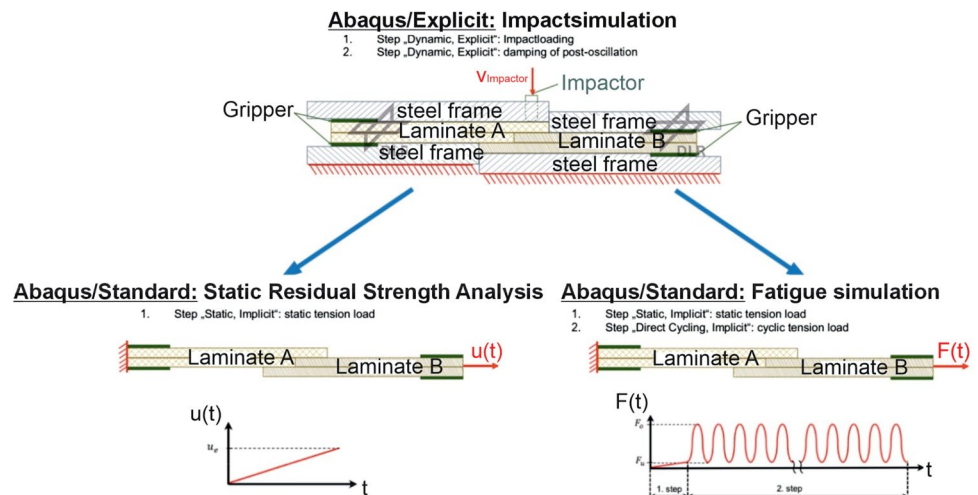
6 Results and discussion

6.1 Calculation procedure

The calculation procedure used can be seen in the Fig. 8. In the first step of the impact simulation, the impact damage is initiated. For this purpose, the impactor is given an initial velocity. The second step serves to dampen the after-swinging and is realised with the load option viscous pressure. The viscous pressure generates a force on the upper and lower surfaces of the lapshear specimen in the opposite direction to the direction of movement. The kinetic energy of the lapshear specimen is thereby largely absorbed, i.e. removed from the energy balance. Subsequently, the lapshear specimen can be imported into the second model almost at standstill. The import includes the material status (of the Hashin damage model and the CZM damage model) and the deformed FE mesh. In the second FE model, the steel frames are removed from the simulation and a static load or a cyclic load is applied to be able to determine the residual static load capacity or the fatigue load capacity. The static residual load capacity simulation and the fatigue residual load capacity simulation differ with regard to the temporal course of the load. In the static residual load capacity model, the displacement is increased linearly on one side up to the maximum value u_e. Here, u_e is sufficiently large so that a complete failure of the Lapshear specimen is ensured. The maximum bearing reaction force is defined as the static residual load capacity. In the fatigue residual load capacity simulation, on the other hand, two load steps are defined. In the first step, the force is increased linearly up to the underload F_u. In the second step, a force-controlled periodic load follows at a defined R-ratio of 0.1. The force at the end of the first step corresponds to the force at the beginning of the second step.

In the course of the evaluation, it became apparent that the impact model cannot be imported into an Abaqus/Standard model due to the high dynamics. Due to this problem, the calculation process is implemented in Fig. 9.

In the implemented calculation procedure, the impact simulation and the static residual capacity simulation are carried out together in an Abaqus/Explicit FE model. For this purpose, a 3rd step is added in which new support conditions are defined and the contacts between the steel frame and the lapshear specimen are deactivated. In the 4th step, the displacement is applied quasi-statically to keep dynamic effects low. The fatigue residual capacity simulation, on the other hand, cannot be carried out with the direct cycling step in Abaqus/Explicit according to the current state of the art. However, the application of the direct cycling-step is necessary with the number of cycles to be applied in order to be able to simulate the fatigue behaviour with permissible calculation time. Consequently, the fatigue residual capacity simulation must be carried out in an Abaqus/Standard model. It is assumed that the fatigue residual capacity of the lapshear specimen is significantly determined by the failure between laminate A and laminate B. For this reason, the detached nodes from the impact simulation are defined as the initial crack in the fatigue residual capacity simulation.

6.2 Geometry approximation and material modelling

The lapshear specimen is a single lap joint (see Fig. 10) consisting of two laminates (laminate A and laminate B) with identical UD stacking sequence. Both laminates consist of twelve layers each with a $[+45/-45/+90/0/-45/+45]_S$ structure, resulting in almost quasiisotropic properties in the layer plane. The grippers have a high coefficient of friction compared to steel and are used for homogeneous load transfer. The grippers consist of two GRP layers with a $[-45/+45]$ structure. The individual layers of the grippers are represented in the model structures as one geometric

Fig. 9 Implemented calculation procedure for the investigation of the static residual load-bearing capacity and the fatigue residual load-bearing capacity after impact loads
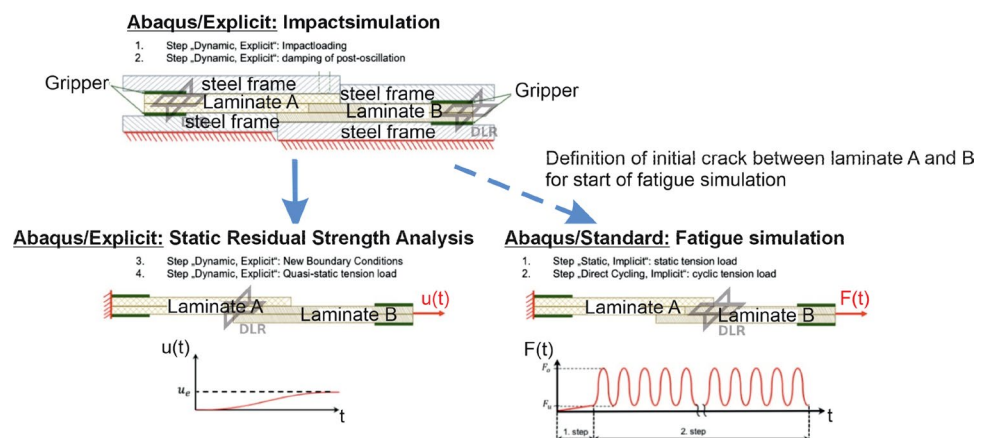
Fig. 10 Sketch of lapshear specimen geometry
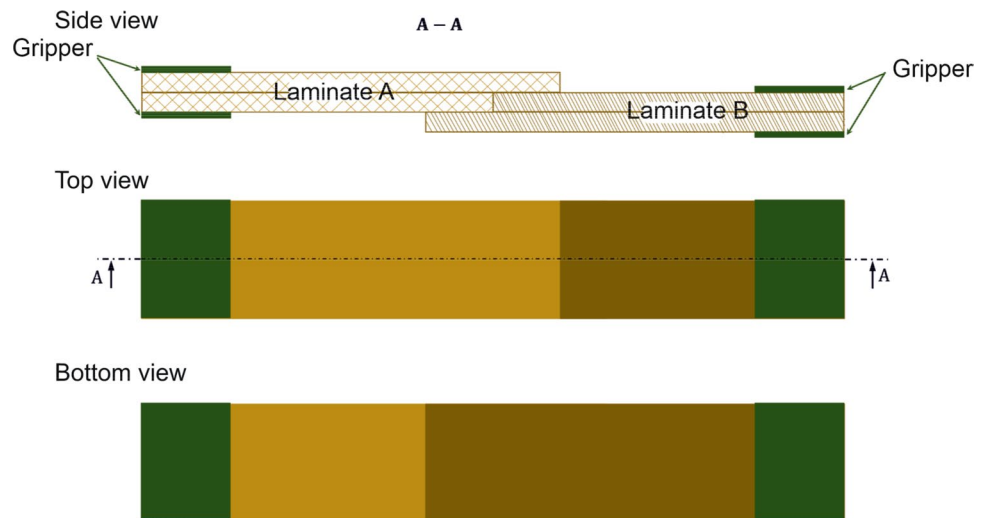
Fig. 11 Sketch of lapshear specimen including steel frames
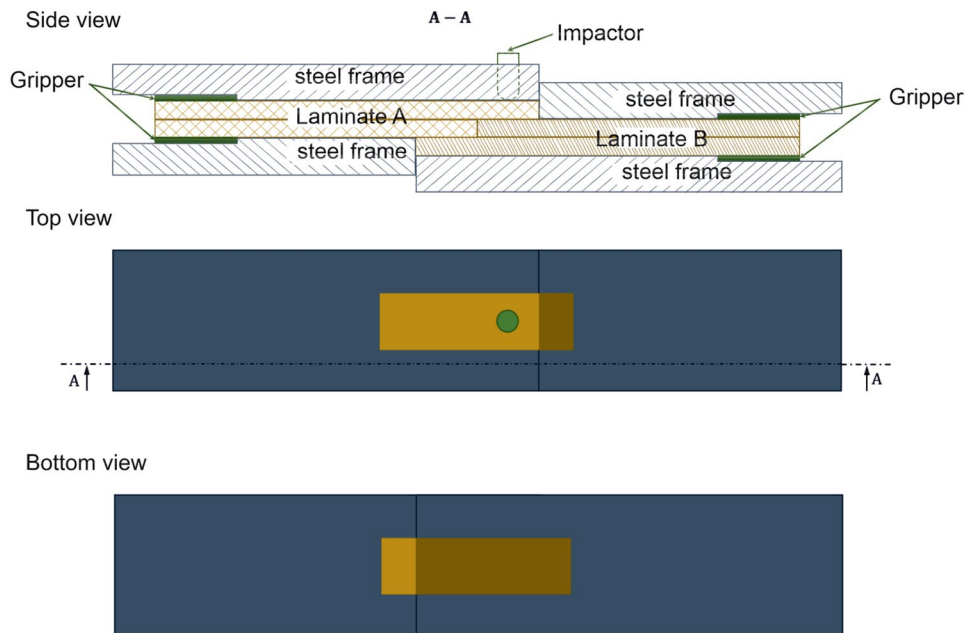
Table 1 Material parameter

Part	Behaviour	Sym. class	E [MPa]	ν [-]
Impactor	Linearly-elastic	Isotropy	210000	0,3
Steel frame	Linearly-elastic	Isotropy	210000	0,3

layer. In contrast, the UD individual layers of the laminates are all mapped geometrically individually.

The lapshear test specimen is produced using a co-consolidation process. This means that the creation of both laminates and the material bond between all joining partners is realised in one process step. The material bond is achieved by a diffusion process in the molten aggregate state of the thermoplastic matrix and the subsequent solidification. The

assembly can be seen schematically in Fig. 11. The geometry of the impactor results from a hemisphere and a cylinder. The diameter of the impactor is chosen in such a way that Barely Visible Impact Damage (BVID) is initiated.

For the impactor and the steel frames, properties of classical structural steel are defined. Accordingly, the impactor and the steel frames are defined as having homogeneous properties with linear–elastic material behaviour that follows the isotropic elasticity law, Table 1.

The UD layers of the laminate consist of UD carbon fibres and an LM-PAEK[2] matrix. A linear-elastic material behaviour with orthotropic elasticity law and homogeneous properties is defined for the UD layers and the grippers, Table 2.

_____
[2] LM-PAEK - "Low-Melt Polyaryletherketone"

Table 2 Material parameter

	E_x [MPa]	E_y [MPa]	E_z [MPa]	G_{xy} [MPa]	G_{xz} [MPa]	G_{yz} [MPa]
UD-layer	143000	8800	10300	4300	4100	4100
Gripper	45000	12000	12000	4400	4400	4400
	v_{xy} [-]	v_{yz} [-]	v_{xz} [-]			
UD-layer	0.35	0.35	0.45			
Gripper	0.25	0.25	0.35			

Table 3 Damage initiation strength parameter and damage evolution parameter to define the Hashin damage model

Longitudinal tension X^L [MPa] EN 2561B	Longitudinal compression X^C [MPa] EN2850B1	Transverse tension Y^T [MPa] EN 2597B	Transverse compression Y^C [MPa] EN2850B1	Longitudinal shear S^L [MPa] AITM 1-0002	Transverse shear S^T [MPa] AITM 1-0002
2769	1765	78	249	141	72
Softening	Longitudinal tension $G_{ft}^C \left[\frac{mJ}{mm^2} \right]$	Longitudinal compression $G_{fc}^C \left[\frac{mJ}{mm^2} \right]$	Transverse tension $G_{mt}^C \left[\frac{mJ}{mm^2} \right]$	Transverse compression $G_{mc}^C \left[\frac{mJ}{mm^2} \right]$	
linear	91.6	79.9	0.22	1.1	

Fig. 12 Meshed assembly for impact simulation and residual strength analysis
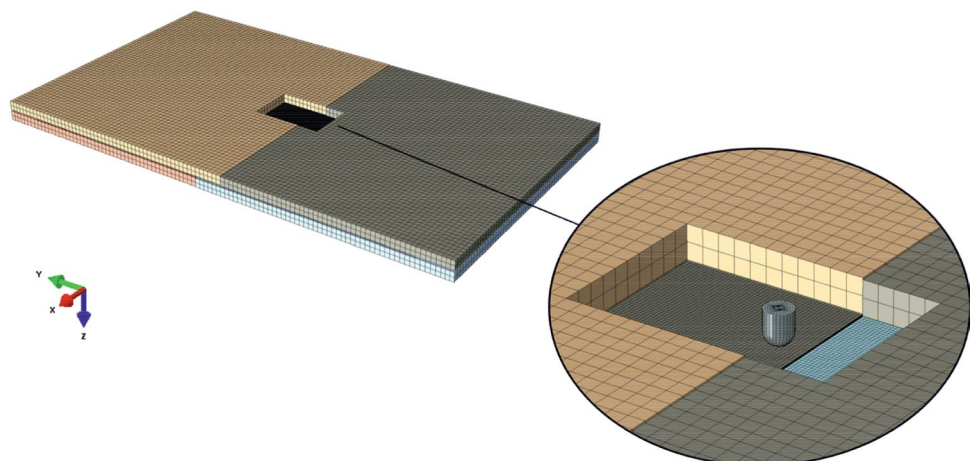
An intralaminar damage model is assigned to the UD layers, Table 3. In Abaqus, the Hashin damage model exists for this purpose, which has been explicitly implemented for laminates. The values were experimentally determined according to Table 3.

Continuum shell elements were used to mesh the individual parts, Fig. 12. For the elements, the option enhanced is activated under Hourglass Control, since the evaluation revealed a high artificial strain energy, which is an indication of hourglassing. In addition, element deletion is activated for the continuum shell elements and the max. degradation value is reduced from 1 to 0.999 as well as a viscosity of 0.001 is introduced to increase the numerical stability after the failure of the Lapshear specimen. The unidirectional layers are cut in order to be able to carry out a mesh refinement close to the impact, Fig. 13, and at the same time to keep the increase in the calculation effort as small as possible. This is because a high quality of results is only required at the impact area, as this area is considered critical to failure due to the impact load.

The number of degrees of freedom must be reduced in the cyclic residual capacity models, Fig. 14, otherwise the calculations would take too long. One of the measures is to reduce the mesh fineness of all individual layers, except for a single layer at which the initial crack is defined. The reduction of the mesh fineness has a negligible influence

Fig. 13 Meshing of lapshear-model for impact simulation and quasi-static residual strength analysis
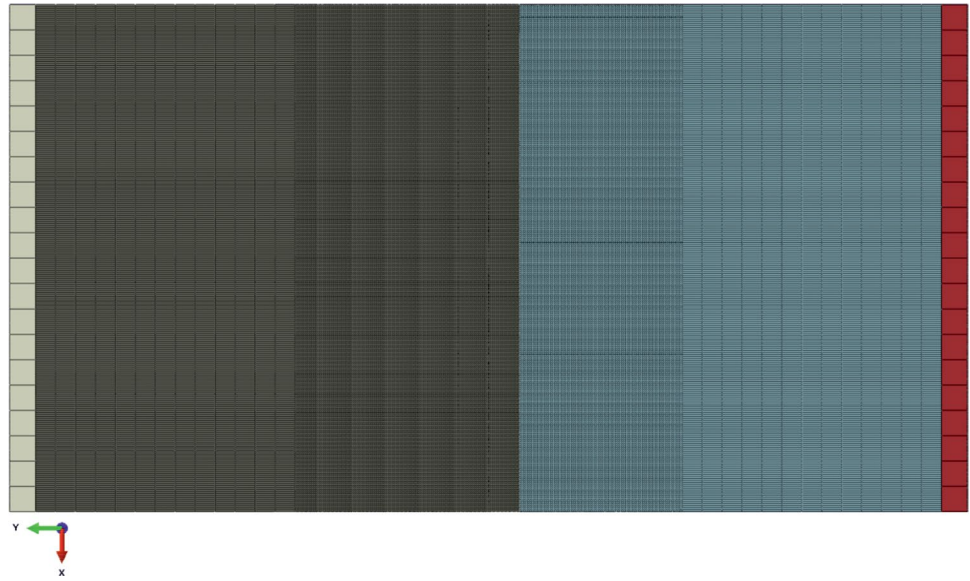
Fig. 14 Meshing of lapshear model for cyclic residual strength analysis
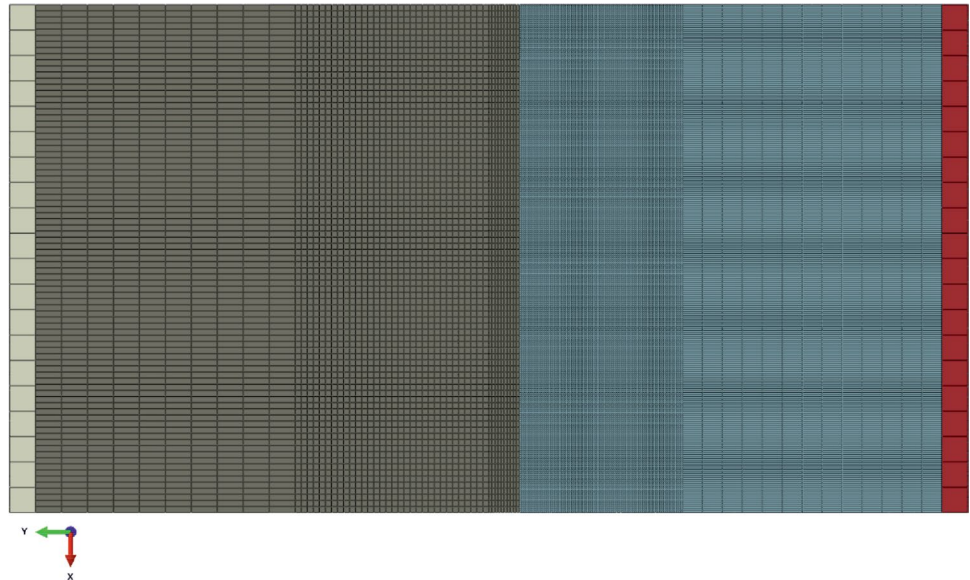
Table 4 Contact conditions for impact simulation and quasi-static residual strength analysis

Slave	Master	Normal direction compression	Normal direction tension	Tangential direction
Gripper	Steel frame	Hard contact	–	Friction $\mu = 0.5$
Gripper	Laminate A/B	Tie	Tie	Tie
Laminate A/B	Steel frame	Hard contact	–	Friction $\mu = 0.5$
Laminate A	Laminate B	Hard contact	CZM	CZM
UD-Layer	Impactor	Hard contact	–	Friction $\mu = 0.5$

on the deformation state of the lapshear specimen[3]. Due to the simplification made, the force flow in the lapshear specimen is inaccurately mapped, as the tie contact definition must be assigned to all nodes. It is not possible to disregard the detached nodes in the tie contact assignment in the cyclic residual capacity model, as the node IDs of

[3] In preliminary investigations for both quasi-static and cyclic models, an element edge length of 2 mm in the overlap and impact regions proved to be a good compromise between computational effort and result quality. This mesh refinement was maintained for the quasi-static models up to 40% of the total specimen length before the mesh was coarsened due to computational time constraints. For the cyclic models, mesh coarsening was implemented significantly earlier to reduce computation time.

Table 5 Bi-linear mixed-mode CZM for characterization of the interlaminar damage

		Strength [MPa]		
Damage initiation	**Damage initiation criterion**	**Fracture mode I** t_n^0	**Fracture mode II** t_s^0	**Fracture mode III** t_t^0
	Quadratic traction	36	80	80
		Fracture energy $[\frac{mJ}{mm^2}]$		
Damage evolution	**Softening:**	**Mixed-mode fracture criterion:**	**Power-law exponent:**	
	linear	power-law	1	
	Fracture mode I G_n^C AITM 1-0005	**Fracture mode II** G_s^C AITM 1-0006	**Fracture mode III** G_t^C AITM 1-0006	
	1.493	2.5	2.5	

Table 6 Parameters of the Paris–Erdogan-Law used for cyclic residual strength analysis, [22]

c_1 $\left[\frac{\text{cycle}}{(\text{MPa·mm}^2)^{c_2}}\right]$	c_2 [−]	c_3 $\left[\frac{\text{mm/cycle}}{(\text{MPa·mm}^2)^{c_4}}\right]$	c_4 [−]	$\frac{\Delta G_{thres}}{\Delta G_c}$ [−]
1	0	20.89	6.05	0.197
$\frac{\Delta G_{pl}}{\Delta G_c}$ [−]	$\Delta G_{I,c}$ $[\frac{mJ}{mm^2}]$	$\Delta G_{II,c}$ $[\frac{mJ}{mm^2}]$	$\Delta G_{III,c}$ $[\frac{mJ}{mm^2}]$	η [−]
0.9	0.212	0.774	0.774	2.1

the cyclic residual capacity models and the impact models differ due to the changed meshing. The refinement at the overlap area is made so that the curvature, which occurs due to the eccentric load application, can be well represented.

The contact conditions used within the numerical simulations are listed in Table 4. It can be seen from the table that CZM contacts (via contact elements) are assigned both between laminate A and laminate B and between the individual UD layers. Here, the cohesion zone model is only defined at the area close to the impact where the finer cross-linking has been done. Outside the finely meshed area, "tie" contacts are assigned. This minimises the computational effort and is permissible since contact detachment due to impact damage is most likely to occur near the impact. The quantities used to characterise the cohesive zone model (CZM) are recorded in Table 5. The parameters used for the Paris–Erdogan-Law are listed in Table 6. The Benzeggagh–Kenane (BK) law is used as mixed-mode behaviour and the default value 0.2[4] is chosen for the tolerance value f_{tol}.

6.3 Impact loading

The curved area of the lapshear specimen is limited by the recess of the steel frame, Fig. 15. This is because the lapshear specimen can only bulge in the area of the recess. At areas where the lapshear specimen is in contact with the steel frames, the curvature and thus also the arching is prevented. The deformation state is qualitatively very similar in all impact models and differs slightly in quantitative terms. The maximum deflection of the lapshear specimen is up to 0.3 ms at the contact to the impactor. After that, the location of the maximum deflection shifts to the left edge. In addition, the dimension of the maximum deflection decreases, which is caused by the fact that the impactor moves upwards again. From 0.4 ms, the location of the maximum deflection shifts again in the direction of the contact area (to the right).

Resistance is provided to the curvature of the lapshear specimen, which is why the speed of the impactor is successively reduced after the impact until it comes to a standstill. The deformation resistance results, on one hand from the frictional connection between the lapshear specimen and the steel frame at the clamping points. On the other hand, the deformation resistance results from the axial section modulus of the lapshear specimen as well as from inertia effects. During the impact of the impactor, part of the initial kinetic energy is converted into deformation energy or elastic energy of the lapshear specimen. The elastic energy causes the impactor to accelerate from its rest position back to its original position, as can be seen in Fig. 16 from 0.3 ms.

---

[4] At has been investigated in previous calculations, the default tolerance value f_{tol}=0.2 for the Benzeggagh–Kenane law ensures numerical stability and an efficient convergence scenario during the simulation of composite material fracture. It is the most valid compromise between computational efficiency and accuracy, allowing energy release rates to be calculated within an acceptable range for the application shown here.

Fig. 15 Deformation in the area of impact event with 35 J impact energy
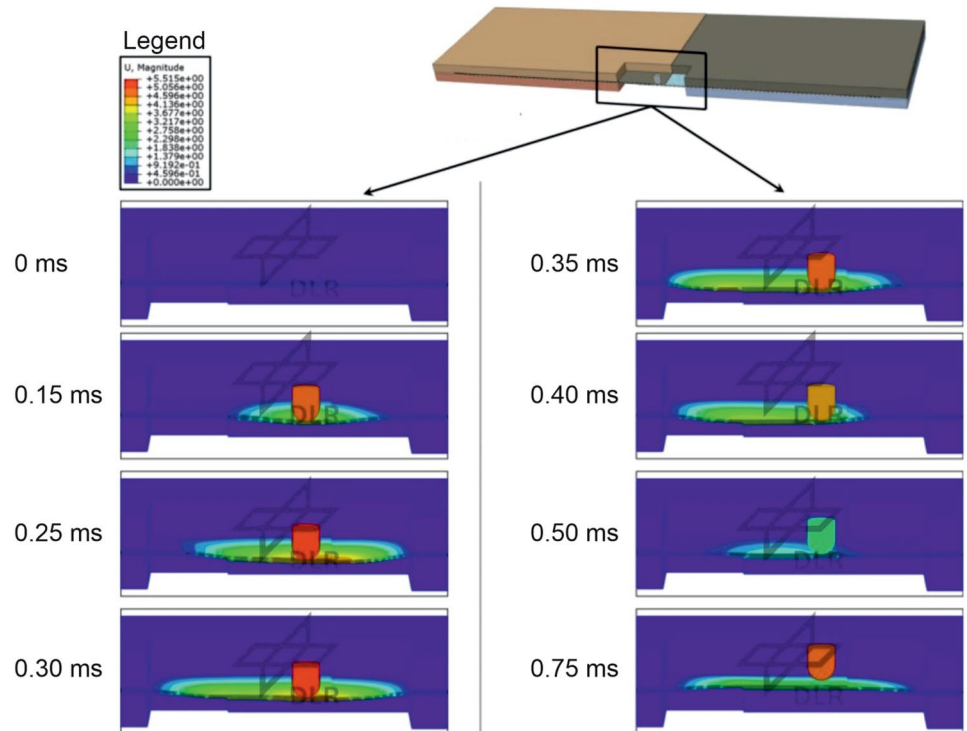
6.4 Interlaminar damage

The contact area between laminate A and laminate B is several times smaller compared to other contact areas between which an interlaminar damage model has been defined, Fig. 17. This is a strong indication that the maximum transmissible force between laminate A and laminate B is the lowest of all contacts. For this reason, this contact area is the most critical for failure. Complete delamination between laminate A and laminate B leads to failure of the entire lapshear specimen. The extent of delamination is therefore of particular importance at this contact area and is therefore illustrated in Fig. 18. The

Fig. 16 Displacement and velocity of impactor in z-direction as function of time
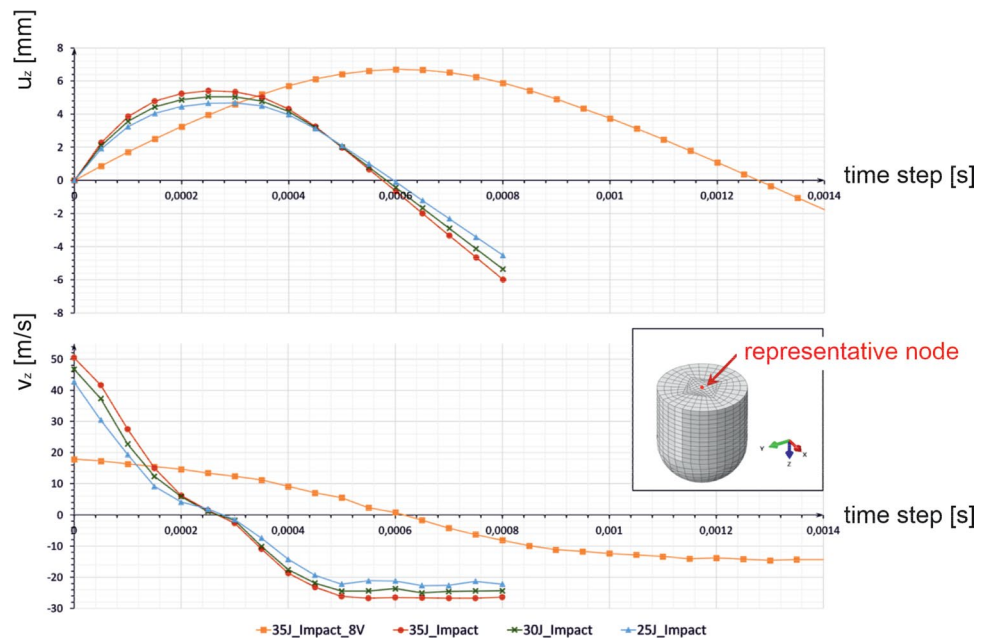
Fig. 17 Lapshear specimen (lower) as well as contact area between laminate A and B (upper)
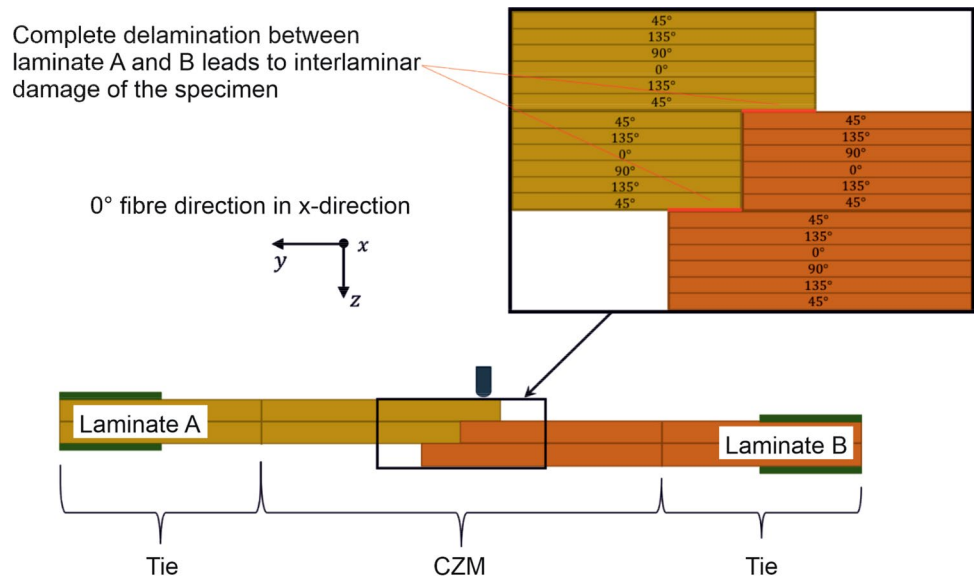
Fig. 18 Interlaminar damage pattern between laminate A and B after impact loading with different energies

red areas indicate complete delamination, while the blue area illustrates damage-free areas. Values between one (red areas) and zero (blue area) characterise the extent of partial damage.

6.5 Intralaminar damage

For the investigation of intralaminar damage, the lapshear specimen is divided into four sub-areas, Fig. 19, laminate A
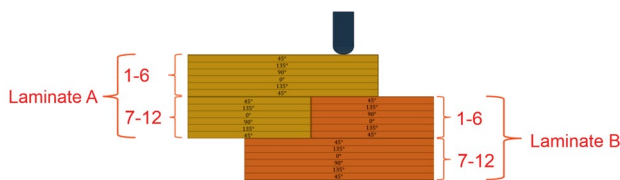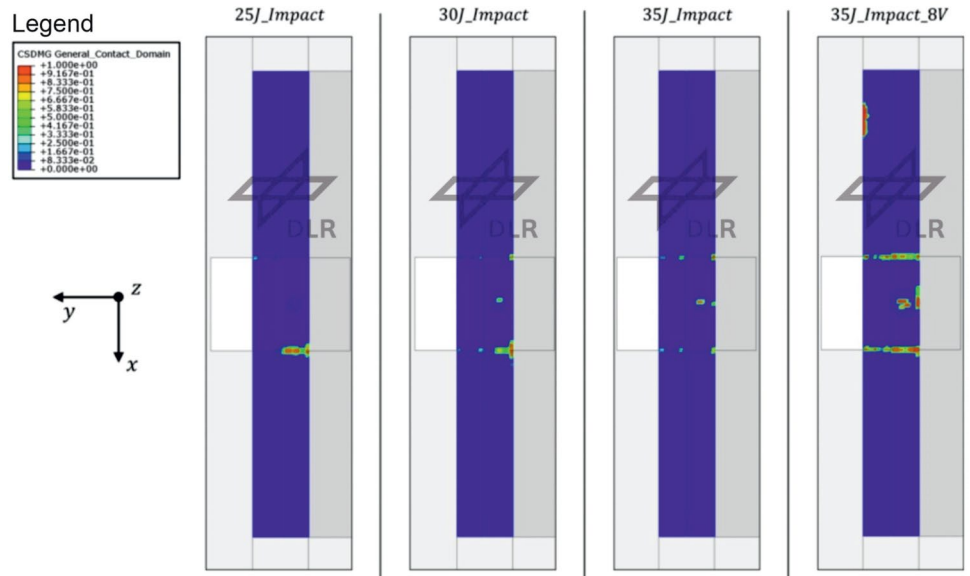
Fig. 19 Subdivision of the lapshear specimen into four sub-areas for a more detailed examination of the intralaminar damage in the lapshear specimen
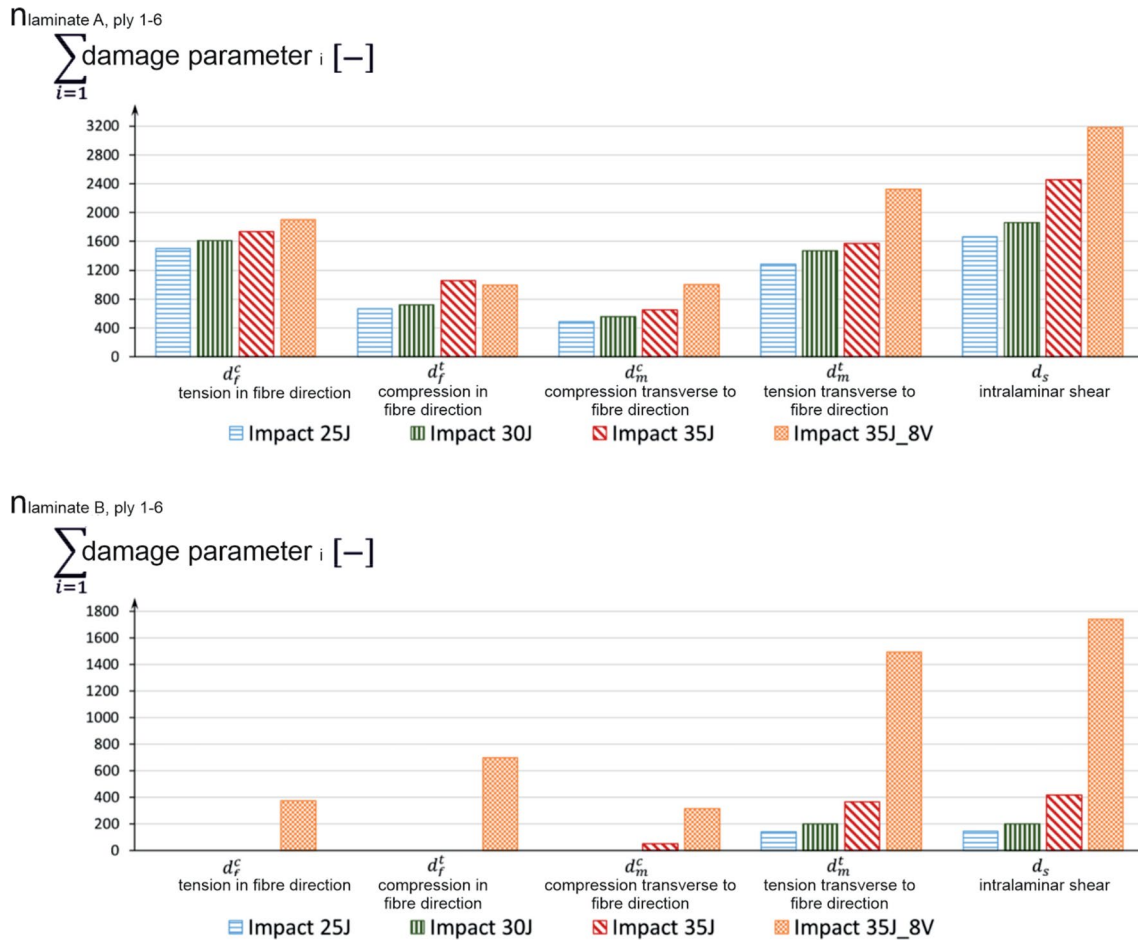
Fig. 20 Damage in layers 1 to 6 of laminate A (upper) and laminate B at different impact energies

and laminate B, and additionally into Layer 1–6 and Layer 7–12. The five damage parameters d_f^c, d_f^t, d_m^c, d_m^t and d_s of the Hashin damage model are used to assess intralaminar damage. These node-based output variables take a value between 0 and 1 and determine the degree of elasticity reduction until complete failure of the continuum. The sum of the damage parameter values of all nodes within a sub-area represents the comparative quantity. It is assumed that this comparative parameter reflects the damage in the corresponding sub-area. In Fig. 20, the damage for layers 1 to 6 of laminate A and laminate B is compared. It can be seen that the damage from layer 1 to 6 in various spatial directions is higher for laminate A than for laminate B. This is due to the direct contact of the impactor with laminate A. The damage is also higher for laminate B than for laminate A. Another reason for the lower damage in layers 1 to 6 of laminate B is the significantly closer position to the neutral fibre. Another finding is the increasing damage with increasing impact energy. Remarkable is the non-existing damage in fibre direction at Impact 25J-, Impact 30J- and Impact 35J-loading. In the case

of Impact 25J and Impact 30J loading, there is also no damage transverse to the fibre direction for areas exposed to pressure. Furthermore, a lower impactor velocity and a larger impactor mass at the same kinetic energy leads to more damage. This finding is provided by the comparison of the damage between the Impact 35J load and the Impact 35J_8V load. The greater damage with the Impact 35J_8V load is probably due to the greater momentum of the impactor. Of all the sub-areas, layers 7 to 12 of laminate B experience the greatest damage, Figs. 20 and 21. Layers 7 to 12 of laminate A are also in contact with steel frame edges. However, the force flow runs to a much lesser extent through this sub-area, so that the pressure and thus the damage is not as pronounced as in layers 7 to 12 of laminate B. In addition, this sub-area is much closer to the neutral fibre. For these reasons, the damage in layers 7 to 12 of laminate A is considerably less than in layers 7 to 12 of laminate B, Fig. 21. Remarkable is the decreasing damage in layers 7 to 12 of laminate B with increasing impact energies, Fig. 21. One possible reason is that the stress concentration at the contact to the impactor is stronger at higher kinetic energies. This
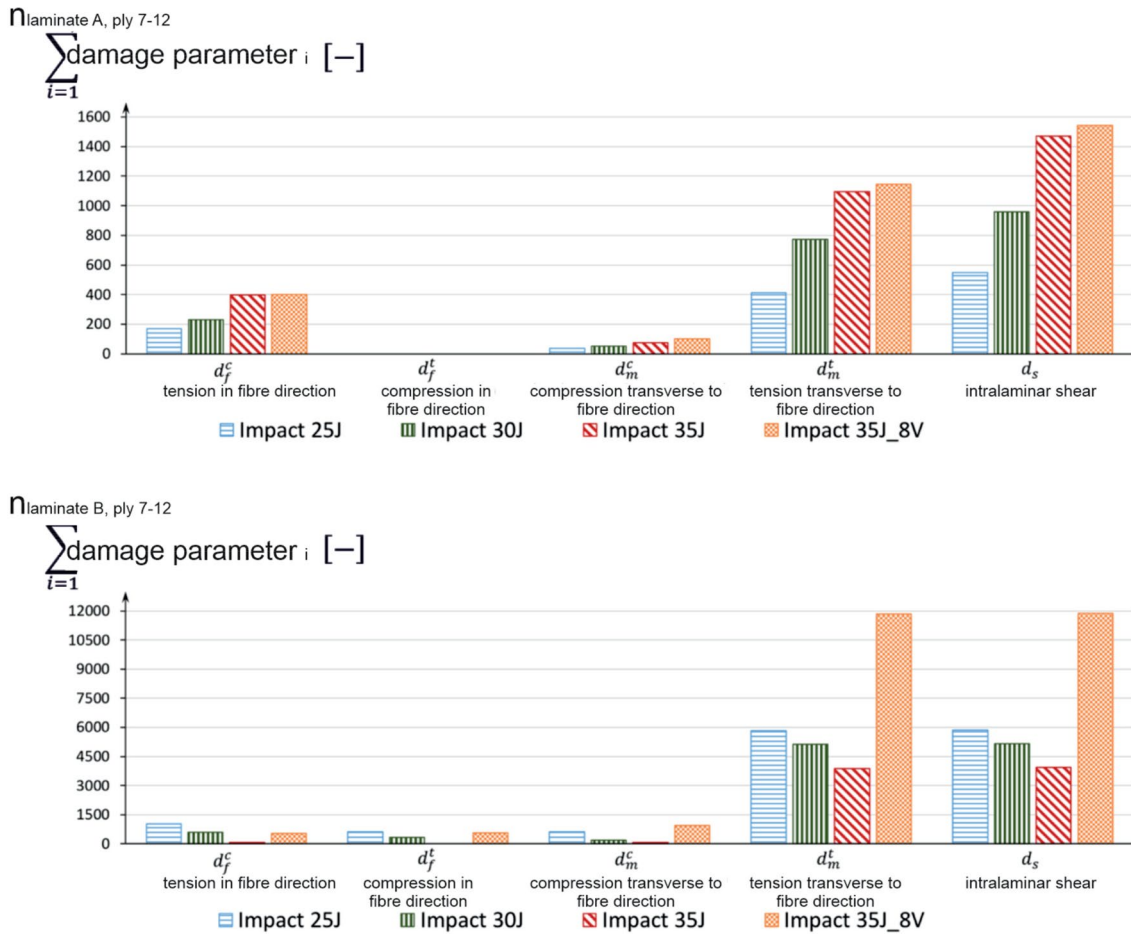
Fig. 21 Damage in layers 7 to 12 of laminate A (upper) and laminate B at different impact energies
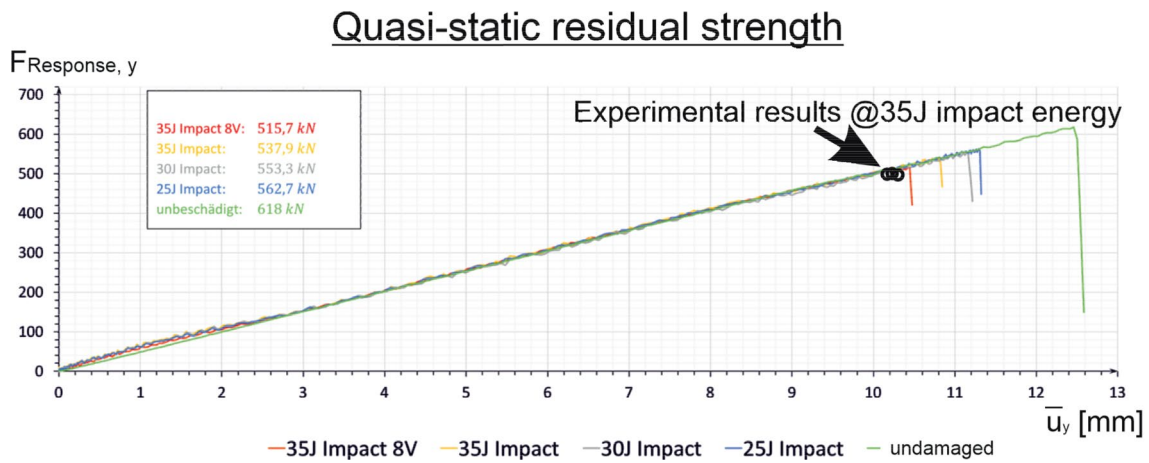
Fig. 22 Quasi-static reaction force versus displacement curves versus experimental results at 35 J impact energy
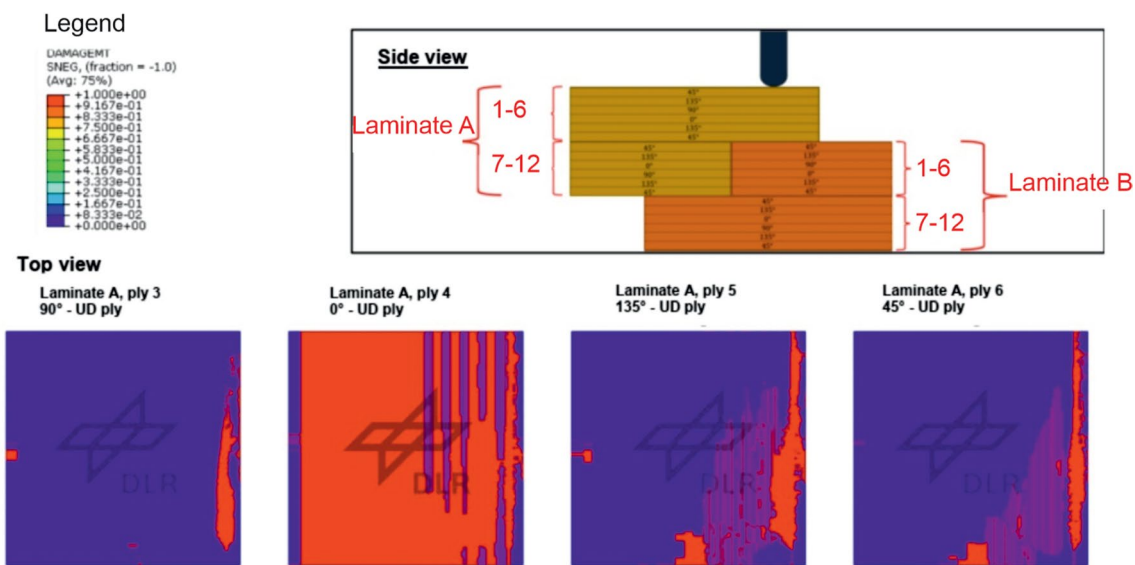
Fig. 23 Intralaminar damage due to transversal tension loading in four unidirectional layers of undamaged lapshear specimen after final failure at 12,58 mm displacement

leads to a stronger local penetration or damage of the lapshear specimen and to a less pronounced bulging of the lapshear specimen. As a result of less bulging, there is less pressure on the steel edge, which ultimately leads to less overall damage.

6.6 Quasi-static residual strength analysis

The static load capacity is defined as the maximum force that the lapshear specimen can oppose to a forced deformation or displacement. To determine this load-bearing capacity, the reaction force is compared with the displacement in the y-direction. The reaction force used results from the sum of

$$F_{\text{Response, y}} = \sum_{i=1}^{n} F_{\text{Bearing, Node } i}. \tag{22}$$

The output displacement is the average node displacement of the loaded edges in the y-direction, which is given by the expression

$$\bar{u}_y = \frac{1}{n} \sum_{i=1}^{n} u_{\text{Loading, Node } i}. \tag{23}$$

The $\bar{u}_y - F_{\text{Response, y}}$ curves reveal an extremely low degree of non-linearity. This is because the curves of the lapshear specimens exposed to impact and the curve of the non-predamaged lapshear specimen have an approximately linear course, Fig. 22. Above a certain load, a drop-in load-bearing capacity can be observed. This decrease in load-bearing capacity is very rapid. The static load capacity of the

undamaged lapshear specimen is clearly the highest at 618 kN. An impact of 25 J leads to a load capacity reduction of 9 % to 562.7 kN. In contrast, an impact of 35 J is associated with a load capacity loss of 13 % to 537.9 kN. An impact of 35 J at 8 times the impactor volume leads to the greatest loss of load capacity by 16.6 % to 515.7 kN. The curves of the lapshear specimens exposed to impact show fluctuations compared to the curves of the reference specimen.[5] These fluctuations are due to the oscillation after the impact load. The higher reaction forces at low displacements of the impact-exposed lapshear specimens are remarkable. The higher reaction forces result from the damping forces that additionally act due to the post-swinging. As the oscillation subsides in the course of the simulation, the damping force also decreases. Against this background, the curves converge with increasing displacement.

For the validation of the quasi-static results after impact, three experiments were conducted on lap shear specimens, each subjected to a 35J impact. Overall, all specimens exhibited a uniform failure mode and showed little variation in the determined residual strengths. A direct comparison of the experimental quasi-static results with the simulation results is presented in Fig. 22. It is clearly evident that the determined residual strengths are somewhat lower compared to the simulated 35J impact. In numerical terms, the percentage deviation is approximately −9.5%, thus currently representing a slightly non-conservative result.

---

[5] not pre-damaged.
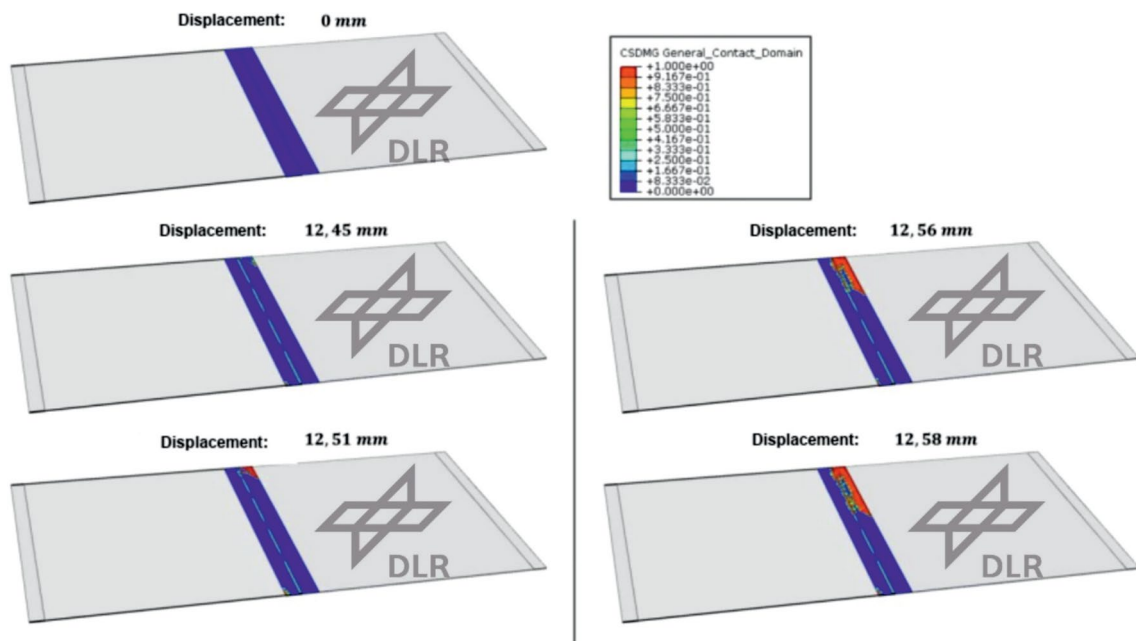
Fig. 24 Interlaminar damage patterns of undamaged lapshear specimen at different displacements

6.7 Intralaminar and interlaminar damage

The first intralaminar damage is initiated at a tensile load of approx. 375 kN in the 0° plies. This is in line with expectations, as the 0° UD plies are predominantly stressed transversely to their fibre direction and there is extremely low strength in this spatial direction. With further load increase, damage occurs simultaneously in the 45° UD plies and the 135° UD plies. In the 90° UD layers, damage is initiated last. The intralaminar damage in all individual layers is almost exclusively caused by a tensile stress transversal to the fibre direction. Compressive stresses transverse to the fibre direction, as well as tensile and compressive stresses in the fibre direction, lead to almost no damage. Consequently, the intralaminar damage is determined by the tensile stress transverse to the fibre direction.
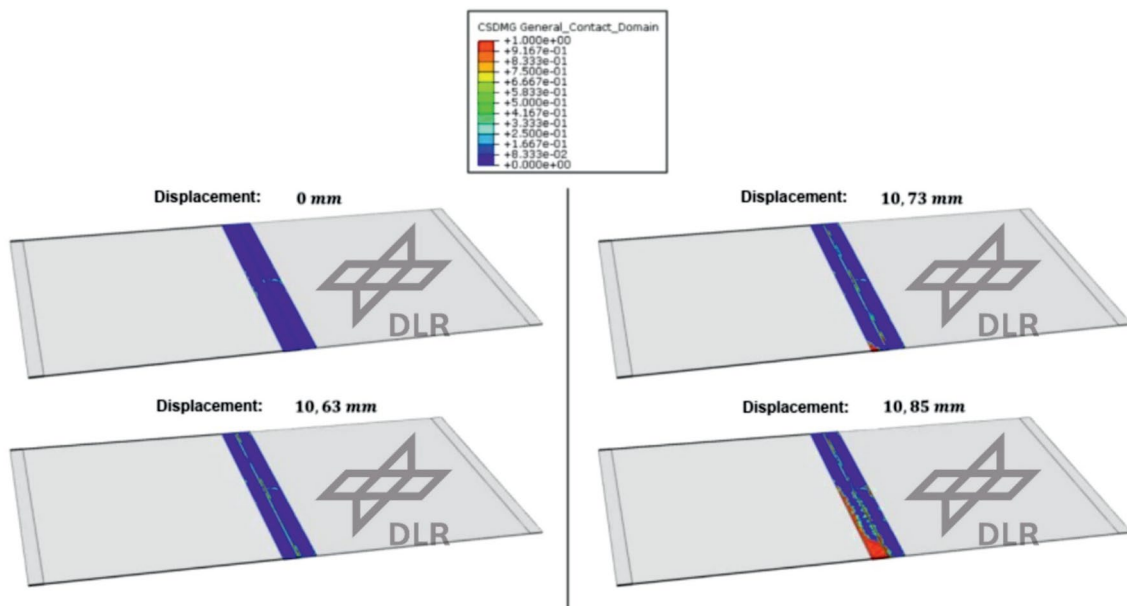
Fig. 25 Interlaminar damage patterns at 35 J impact energy at different displacements

Figure 23 shows the extent of intralaminar damage in four differently oriented layers caused by tensile stress transverse to the fibre direction. Each damage pattern represents, to a good approximation, the damage of a similarly oriented UD layer within the lapshear specimen. The extent of intralaminar damage is highest in the 0° UD layers, followed by the 135° oriented UD layers and the 45° oriented UD layers. The extent of damage is lowest in the 90° UD layers, as this layer is predominantly subjected to stress in the fibre direction. In all layers, damage is present in the overlap area. When damage occurs, the load is redirected over undamaged areas. The decrease in load-bearing capacity of the undamaged Lapshear specimen in Fig. 22 is not due to intralaminar damage, but to interlaminar damage. An indication of this is provided by interlaminar damage patterns, Figs. 23 and 24. Up to a displacement of 12.45 mm, almost no interlaminar damage is

evident. From 12.45 mm, where a decrease in load-bearing capacity is observed, a pronounced increase in interlaminar damage between laminate A and laminate B can be seen.

The damage caused by the impact causes a change in the force flow in the lapshear specimen. The changed force flow leads to a different damage pattern between the non-pre-damaged lapshear specimen and the lapshear specimen exposed to the impact. Despite the deviating force flow, the interlaminar damage is also responsible for the failure or the reduction in load-bearing capacity of the pre-damaged lapshear specimens. This finding is clearly illustrated in Fig. 25 using the example of the 35 J pre-damaged lapshear specimen. The interlaminar damage between laminate A and laminate B only increases visibly from 10.73 mm displacement. From this displacement onwards, a decrease in load-bearing capacity can also be observed, Fig. 22. In this respect, the
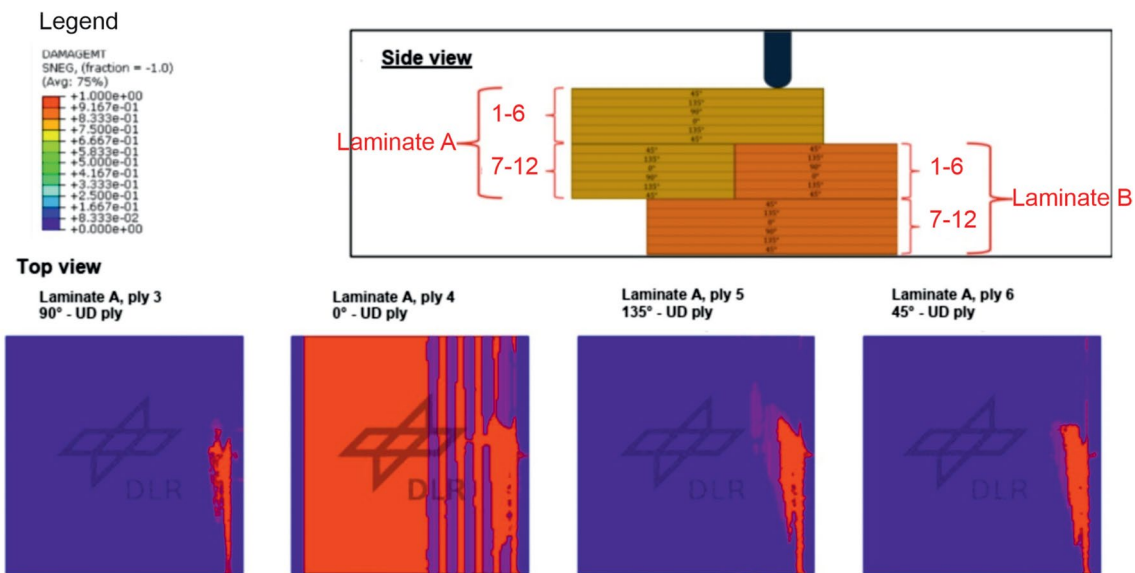
Fig. 26 Intralaminar damage due to tensile stress transverse to the fibre direction in four UD layers of the 35 J pre-damaged lapshear specimen after failure at 10.85 mm displacement
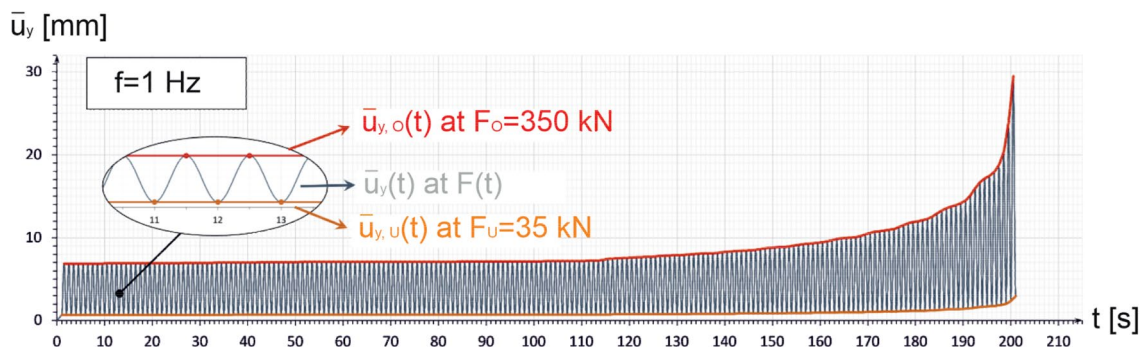
Fig. 27 Displacement patterns at load introduction edges as function of time. R-ratio=0,1, maximum force equals 350 kN

Fig. 28 Number of load changes at different maximum forces
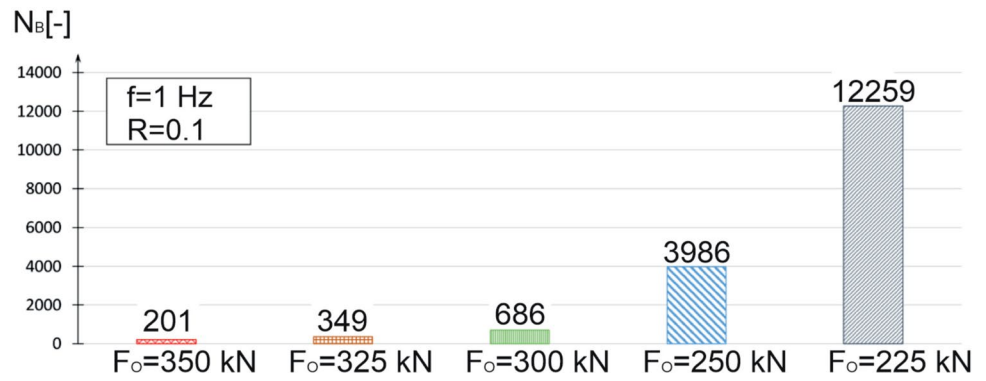
decrease in load-bearing capacity is related to the interlaminar damage between laminate A and laminate B. The interlaminar damage is mainly initiated at the edge, as in the undamaged lapshear specimen, Fig. 24, but on the opposite side. Subsequently, the interlaminar damage spreads towards the centre. Because the interlaminar damage between laminate A and laminate B is significantly more pronounced at lower loads, the Lapshear specimen fails prematurely. For this reason, there is significantly less intralaminar damage, Fig. 26, compared to the Lapshear specimen that is not predamaged, Fig. 23.

6.8 Cyclic residual strength

Figure 27 shows the average displacement of the two loaded edges $\bar{u}_{y(t)}$ plotted against time t. The red curve and the orange curve illustrate the displacement $\bar{u}_{(y,U)}(t)$ at the upper force and the lower force, respectively. From the curves, a softening of the lapshear specimen with increasing number of load cycles can be observed.

The increase in displacement is determined by the crack growth. The stronger the crack growth, the greater the displacements become. If there is no crack growth, the curves take a constant course. For all upper forces, the initial crack grows first (area 1) in the first contact area. After the crack has completely propagated in the first contact area, crack growth begins with a time delay in the second contact area. The extent of the time offset (area 2), in which there is no crack growth and is characterised by the constant course, is determined by the upper force. At the upper force of 350 kN, there is no constant area, as there is constant crack growth. When the crack starts to grow in the second contact area, the displacements increase exponentially within a short time until failure (area 3). The number of load changes until failure differs significantly for different upper forces, Fig. 28. A reduction of the upper force from 350 kN to 225 kN leads to an increase of the number of load changes until failure by
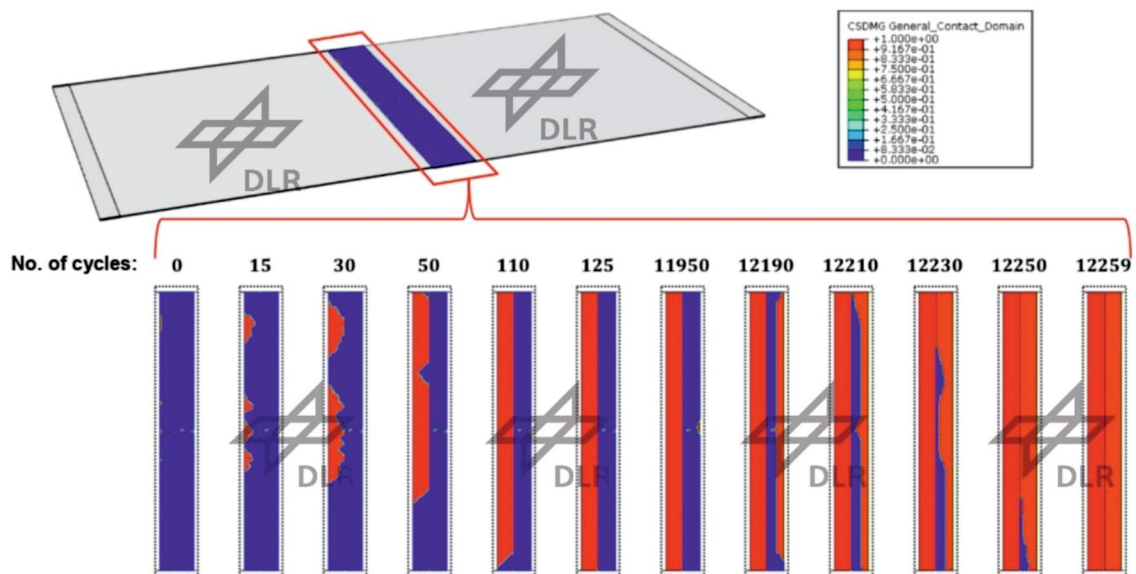
Fig. 29 Interlaminar damage for maximum force of 225 kN and R-ratio of 0,1 after different number of load changes
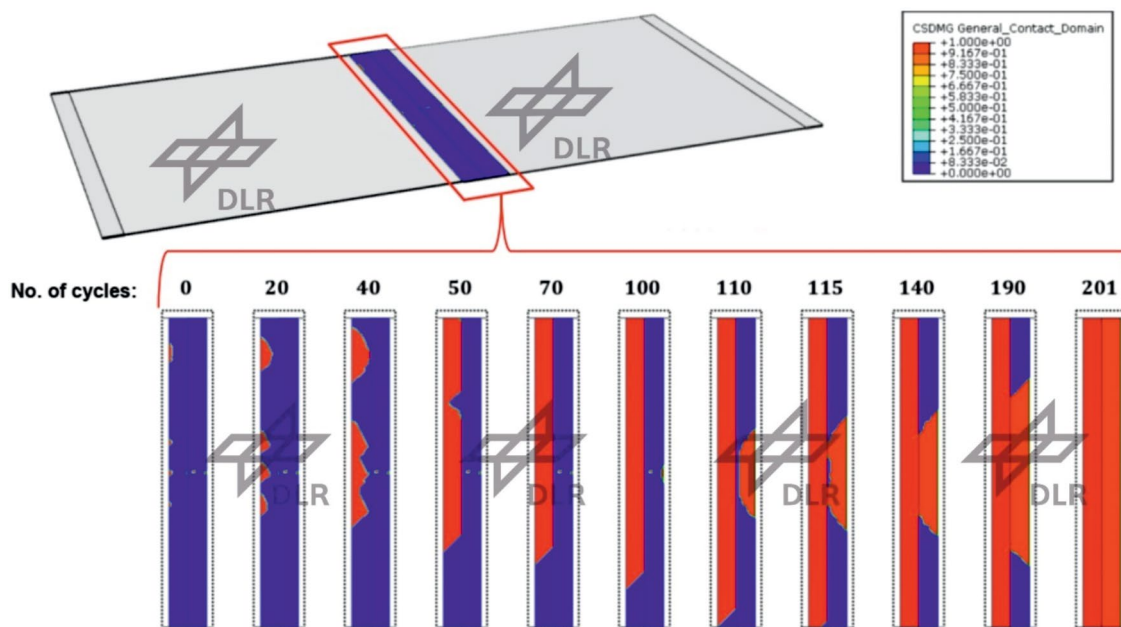
Fig. 30 Interlaminar damage for maximum force of 350 kN and R-ratio of 0,1 after different number of load changes
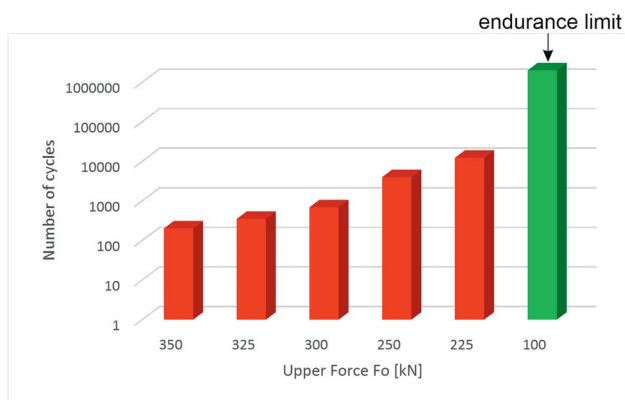
Fig. 31 Numerically obtained residual strength values (red) and experimentally received endurance limit (green)

Fig. 32 Development of stiffness values during cyclic loading. No loss of stiffness can be observed

6000 % ((12259 kN-201 kN)/(201 kN)), from 201 to 12250. At an upper force of 200 kN, there is no crack growth in the second contact surface, theoretically, so the number of load changes until failure is theoretically infinite which is called endurance limit.

6.9 Interlaminar damage of lapshear specimen

The crack growth rate is extremely high after the crack growth criterion has been met. The initial crack spreads rapidly in the first contact area as well as in the second contact area within a relatively low number of load cycles, Fig. 29. After only 125 cycles, the initial crack has completely propagated in the first contact surface at an upper force of 225 kN and an R-ratio of 0.1. Subsequently, almost no crack growth occurs until approx. 11950 cycles. After approx. 11950 cycles, the crack begins to grow in the second contact area. The crack growth is asymmetrical due to the bend-twist coupling, see damage pattern after 12230 cycles. After 12259 cycles, both contact surfaces have completely detached from each other, which is accompanied by a failure of the lapshear specimen. With an upper force of 350 kN, the crack grows faster, as expected. The first contact surface has already

been completely detached after approx. 115 cycles, Fig. 30. From 100 cycles onwards, one of the initial cracks of the 2nd contact surface also grows and has completely propagated after 201 cycles. Compared to Figs. 29, 30 shows a clearly more symmetrical crack growth. Presumably, the load is so high that the crack propagation is shear-dominated, which is why the coupling effect has no visible influence on the crack propagation.

As stated in the previous section, the endurance limit should be maintained at upper force levels below 200 kN. To validate the numerical findings from the fatigue studies, cyclic experimental investigations were also conducted. The objective was to determine the load required to achieve the endurance limit of the specimens. Figure 28 illustrates that as the applied surface force decreases, the number of cycles to failure increases significantly. Based on the numerical findings presented in the previous section and preliminary experimental tests on lapshear specimens, the upper force for the experimental investigations was set at $F_U = 100kN$ to prevent damage to the specimens. Figure 31 clearly demonstrates that this load ensures the endurance limit is reached for the examined specimens. At this upper force, no loss of stiffness was observed in the specimens, even after 2 million cycles (Fig. 32). Therefore, the upper force limit required to achieve the endurance limit lies between the theoretically predicted 200 kN and the experimentally determined 100 kN. The emerging trend in the numerical studies was thus experimentally validated, and the threshold for the surface force required to reach the endurance limit was established.

7 Conclusion and outlook

This investigation assesses the suitability of thermoplastically bonded joints for connecting individual fuselage segments to form an overall structure. The preference for a thermoplastic welding process arises due to significant delays associated with riveted joints during assembly, resulting in economic disadvantages. The implementation of importing the impact state from Abaqus/Explicit into an Abaqus/Standard residual capacity model using Abaqus is not feasible due to high dynamics. Consequently, a methodology is presented for evaluating the static residual and fatigue capacities of the lapshear specimen, considering impact-induced damage. This methodology provides numerical results, enhancing the understanding of interlaminar and intralaminar damage extent, load-bearing capacity, and failure causes. The investigation focuses on the interlaminar damage extent between laminate A and laminate B, crucial for specimen failure. Surprisingly, an inverse relationship is observed between interlaminar damage and impactor kinetic energy, except for the 35J_Impact_8V load. Local damage associated with increased impactor velocity counteracts global deformation,

impacting interlaminar damage. A notable difference in interlaminar damage extent occurs with the same kinetic energy but different impactor volume and speed.

Increasing the impactor volume by factor 8, with a corresponding decrease in initial velocity, results in significantly greater damage, potentially due to differences in momentum. This prompts consideration of momentum, rather than kinetic energy, as a measure of impact load. Future studies should investigate whether the same impulse with varied volume (or mass) and velocity yields similar interlaminar damage. For precise intralaminar damage investigation, four subareas of the lapshear sample are considered, allowing quantification through summation of damage parameters within each subarea. While not an absolute physical quantity, this parameter facilitates comparison within FE models. Simulation of damaged and undamaged lapshear specimens under quasi-static tensile loading reveals an almost linear behavior until rapid failure. Intralaminar and interlaminar damage investigations highlight interlaminar damage as the cause of failure for both specimens. Lapshear specimen load-bearing capacity decreases with increased impactor kinetic energy. Among four impact loads, only one shows node detachment at both contact surfaces between laminate A and laminate B. Impact simulations after one load with a 35 J impactor and 8 times volume reveal a reduction in fatigue residual load capacity. Small changes in load amplitudes significantly influence fatigue capacity, where an upper force increase leads to detachment after a limited number of load cycles. Further determination of material parameters, specifically intralaminar fracture energy and the Paris–Erdogan law, is recommended to enhance numerical calculation results. Additionally, developing a three-dimensional intralaminar damage model can improve the quality of simulations.

Data availability Authors can confirm that all relevant data are included in the article and/or its supplementary information files.

Declarations

Conflict of interest There are no conflict of interest.

References

1. Kreikemeier, J., Abdulkadir, A.: Numerical analysis of thermoplastically welded CFRP structures. Appl. Compos. Mater. **30**, 73–91 (2023). https://doi.org/10.1007/s10443-022-10076-7

2. Gol'denblat, I.I.: Kopnov: Strength of glass-reinforced plastics in the complex stress state. Mekhanika Polimerov **1**, 54–59 (1965)

3. Puck, A.: Festigkeitsanalyse Von Faser-Matrix-Laminaten: Modelle for die Praxis. Carl Hanser Verlag, ??? (1996)

4. Irwin, G.R.: Analysis of stresses and strains near the end of a crack traversing a plate. J. Appl. Mech. **24**, 361–364 (1957)

5. Wells, A.A.: Unstable crack propagation in metals: cleavage and fast fracture. Crack Propagation Symposium, Cranfield **4**, 8 (1961)

6. Dugdale, D.S.: Yielding of steel sheets containing slits. J. Mech. Phys. Solids **8**, 100–104 (1960)

7. Barenblatt, G.I.: Mathematical theory of equilibrium of cracks in brittle fracture. Adv. Appl. Mech. **7**, 55–129 (1962)

8. Needleman, A.: A continuum model for void nucleation by inclusion debonding. J. Appl. Mech. **54**, 525–531 (1987)

9. Xu, X.P., Needleman, A.: Numerical simulations of fast crack growth in brittle solids. J. Mech. Phys. Solids **42**, 1397–1434 (1994)

10. Xu, X.P., Needleman, A.: Numerical simulations of dynamic interfacial crack growth allowing for crack growth away from the bond line. Int. J. Frac. **74**, 253–275 (1995)

11. Camacho, G., Ortiz, M.: Computational modelling of impact damage in brittle materials. Int. J. Sol. Struc. **33**, 2899–2938 (1996)

12. Xu, X.P., Needleman, A.: Void nucleation by inclusion debonding in a crystal matrix. Model. Simul. Mater. Sci. Eng. **1**, 111–132 (1993)

13. Ortiz, M., Pandolfi, A.: Finite-deformation irreversible cohesive elements for three-dimensional crack-propagation analysis. Int. J. Numer. Meth. Eng. **44**, 1267–1282 (1999)

14. Ghosh, S., Ling, Y., Majumdar, B., Kim, R.: Interfacial debonding analysis in multiple fiber reinforced composites. Mech. Mat. **32**, 561–591 (2000)

15. Camanho, P.P., Davila, C.G, Ambur, D.R.: Numerical simulation of delamination growth in composite materials. NASA/TP, 1–24 (2001)

16. Camanho, P.P., Davila, C.G.: Mixed-mode decohesion finite elements for the simulation of delamination in composite materials. NASA/TM, 1–42 (2002)

17. Camanho, P.P., Davila, C.G., Moura, M.F.: Numerical simulation of mixed-mode progressive delamination in composite materials. J. Comp. Mat. **37**, 1415–1438 (2003)

18. Costa, A.P., Botelho, E.C., Costa, M.L., Narita, N.E., Tarpani, J.R.: A review of welding technologies for thermoplastic composites in aerospace applications. J. Aerosp. Technol. Manag. **4**, 255–265 (2012)

19. Barenblatt, G.I.: The formation of equilibrium cracks during brittle fracture general ideas and hypotheses axially-symmetgric cracks. J. Appl. Math. Mech. **9**, 622–636 (1959)

20. Paris, P.: A critical analysis of crack propagation laws. J. Basic Eng. **8**, 528–533 (1963)

21. Benzeggagh, M.: Measurement of mixed-mode delamination fracture toughness of unidirectional glass/epoxy composites with mixed-mode bending apparatus. Compos. Sci. Technol. **2**, 439–449 (1996)

22. Krueger, R., Deobald, L., Gu, H.: A benchmark example for delamination growth predictions based on the single leg bending specimen under fatigue loading. Adv. Model. Simul. Eng. Sci. **7**(1), 1 (2020)

Publisher's Note Springer Nature remains neutral with regard to jurisdictional claims in published maps and institutional affiliations.